Effect of central and non-central frequency components on the quality of damage imaging

Gnana Teja Pudipeddi[1], Ching-Tai Ng[1,*], Andrei Kotousov[2]

[1] School of Civil, Environmental & Mining Engineering, The University of Adelaide, Adelaide, SA 5005, Australia

[2] School of Mechanical Engineering, The University of Adelaide, Adelaide, SA 5005, Australia

Abstract

Accurate image reconstruction of damage through Lamb wave diffraction tomography (LWDT) requires substantial information of scatter field. This can be achieved by using transducer network to collect the scatter field data. However, this requires a large number of transducers that creates logistical constraints for the practical applications of the technique. Various methods have been developed to improve the practicability of LWDT. One of the main approaches is to employ data at multiple frequencies within the bandwidth of the excitation signal. The objective of this study is to investigate the performance of using the data at non-central frequencies to reconstruct the damage image using LWDT. This provides an understanding on the influence of data at each individual frequency in the damage image reconstruction.

In this paper, a series of numerical case studies with consideration of different damage sizes and shapes are carried out. Different non-central frequencies data is used to reconstruct the damage image. The results show that using the data at different non-central frequencies leads to different qualities of the reconstructed damage images. The quality of these reconstructed damage images are then compared to investigate the information contained of the data at each individual frequency. The study shows that the non-central frequencies data can provide additional information in the damage image reconstruction. Overall the results of this study provide insights into the influences of the data at different frequencies, which is essential to advance the developments of the LWDT.

Keywords: Lamb wave, diffraction tomography, imaging, damage identification, structural health monitoring, scattering, multi-frequency

* Corresponding author email: alex.ng@adelaide.edu.au

1. Introduction

Structural health monitoring (SHM) has attracted increasing attention in the last two decades. It enhances reliability and sustainability of structures through providing in-situ structural monitoring. Different damage detection techniques have been developed to provide early detection of damage and reduce the life-cycle costs of the structures. Early developments focused on non-destructive evaluation (NDE) techniques, such as visual inspection [1,2], conventional ultrasonic [3,4], thermography [6] and eddy-current techniques [7,8]. However, safety inspections using these techniques are usually carried during scheduled maintenance and they are not able to inspect inaccessible locations of the structures, as they need to be operated manually by experienced inspectors. In addition the coverage area is usually small in each inspection process. Therefore, the safety inspections using these NDE techniques are time-consuming and cost ineffective, and they are generally not suitable for SHM purposes. It is important to develop a reliable and robust damage detection that can provide in-situ monitoring of the structure. Guided wave based damage detection techniques are feasible for SHM as they are able to provide in-situ monitoring of structures. Additionally, they are sensitive to small and different types of damages, able to inspect inaccessible locations, and cost effective. These advantages make them to be one of the most promising damage detection methods. In the literature, different damage detection methods have been developed used the guided wave [9-12].

1.1. Damage detection using Lamb wave

Lamb waves are mechanical stress wave that propagates along plate-like structures and are guided by structural boundaries. It is a type of guided wave. In the last two decades, Lamb waves have attracted considerable attention [13-17] in SHM. To date, numerous damage detection techniques using Lamb waves have been developed, for example, time-of-flight approach [18], maximum-likelihood estimation [19], damage imaging [20-22], phase array approach [23], model based approach [24,25], time-reversal approach [26] and diffraction tomography [27-29]. Each of these techniques provides different levels of assessment for the damages in the structures. While some methods are only able to determine the existence and location of the damages, some others provide more information, such as severity and shape of the damages.

Recently, developments have been extended to the concept of using the nonlinear guided wave for damage detection [30-34]. This is potential to address some bottlenecks of the linear guided wave approaches, e.g. the need of baseline data, which can be changed under varying temperature and operational conditions [35-37]. This study will only focus on the topic of linear guided wave and diffraction tomography approach.

1.2. Lamb wave diffraction tomography

Apart from the essential requirements that the damage detection must be reliable and sensitive to the damages, two additional features: graphical representation and quantitative identification; can provide invaluable information for SHM. The former provides physical information for engineers in understanding the damage detection results and the latter provides comprehensive information, which can assist decision-making on the remedial work.

Lamb wave diffraction tomography (LWDT) is a quantitative damage detection technique that provides an efficient and cost effective inspection of a large area of structures. It utilizes the scattering effects of Lamb waves and various tomographic algorithms to reconstruct robust images of the damages. The scattered wave field can be obtained by sequentially interrogating an area of interest with Lamb waves using multiple transducers. Early developments of tomographic imaging are based on the time-of-flight information of Lamb waves [38-40] to reconstruct an image of the damage. But this approach assumes that Lamb wave propagation is in the form of straight rays.

Malyarenko and Hinders [27] proposed a diffraction tomography approach that takes into account the diffraction effect of Lamb waves to improve the reconstructed image quality and resolution. Wang and Rose [28,41] proposed a LWDT framework based on the Mindlin plate theory and Born approximation, which relates the scattered plate waves to the damage geometry. The damage parameters were mathematically represented as local perturbations of the global material parameters. The scatter field amplitudes were then found to have a linear relationship with the Fourier transform of these perturbation functions. Hence, once the Fourier transform values of the perturbations were obtained from the scattered field amplitudes, an inverse transformation could be applied to obtain the damage parameters. The framework was further investigated for corrosion damage in isotropic plates [29].

Belanger et al. [42] also proposed a LWDT framework based on the Born approximation. The framework examines the dependence of the phase velocity of the waves, on the plate thickness. The phase velocity of the fundamental anti-symmetric (A_0) mode of a Lamb wave is proportional to the square root of the frequency-thickness product. This implies that for constant frequency, Lamb waves have a lower velocity in the plate regions with reduced plate thickness. Hence, a diagnostic image of the damage can be reconstructed using the wave velocity profile. After that various inverse methods and scattering models were also developed [44,45] to improve damage resolution and the computational efficiency of LWDT.

Development of accurate and simple inverse transformation techniques that do not require a large number of transducers for LWDT is a very important topic of research. In addition to the two-dimensional (2D) Fourier transformation approach that was originally used for early development of LWDT, Devaney and Dennison [46] proposed a least-squares estimation method for inverse

transformation. The least-squares estimation method was implemented by Rohde et al. [47] using a constrained linear inversion technique and the results were found to be more accurate and have better performance than the direct Fourier inversions approach.

One of the major requirements of the technique proposed by Wang and Rose is the assumption that the scatter field data collected is under far-field conditions [28,41,43]. That is, the distance between the sensors and the damage is greater than $2d^2/\lambda$, where d is the diameter of the damage and λ is the wavelength of the Lamb wave. However, a near-field imaging method is more practical as the damage may be closer to the transducer in real life applications. This drawback was addressed by Chan et al. [50] where they employed finite element based numerical Green's functions and the multi-static data matrix to overcome this constraint. The Green's functions can be defined as an undamaged structure's response to a unit input. They also showed that the numerical method suggested for the calculation of Green's functions is in agreement with the analytical function [41]. A similar numerical method, which significantly reduces the mathematical intensity of the solution, was also developed for the evaluation of the multi-static data matrix. They proposed that the Green's function can be estimated by the ratio of the Fourier transforms of the response and the input forces at the central frequency.

In general, the excitation signal for a Lamb wave is a narrowband signal, which contains multiple frequency components. While the central frequency of this signal is predominant and has the maximum amplitude in the Fourier transform of the signal, it can also be observed that the wave-field also contains a significant number of frequency components adjacent to the central frequency. A multi-frequency approach that incorporates the effects of the non-central frequencies in damage image reconstruction was proposed by Belanger et al. [42]. However, the effect of the non-central frequency components on the quality of the reconstruction damage imaging has not yet been examined. The aim of this paper is to examine the quality of the reconstructed damage image using LWDT based on the Mindlin plate theory and Born approximation when the non-central frequency components of response signals are used in the image reconstruction.

This paper aims at addressing the importance and efficiency of non-central frequencies in the reconstruction of the damage image. The non-central frequency components have a two-fold advantage in the advancement of the LWDT. Firstly, they reduce the number of transducers by using data from multiple frequencies, and consequently the implementation costs. Secondly, they also improve the damage resolution by gathering additional data from the same number of transducers, and hence, this gives a better image resolution. This study provides a comprehensive assessment of the non-central frequencies on the performance of the reconstructed damage image using diffraction tomography algorithm. The quality of the reconstructed damage images using central and non-central frequency data are compared. This provides an examination of the quality of

the reconstructed damage image using LWDT when the non-central frequency components of response signals are used in the image reconstruction.

The paper is structured as follows: Section 2 describes the methodology of the near-field imaging algorithm. Section 3 presents the FE model in the numerical simulations and describes the details of the numerical case studies. The results and discussions can be found in Section 4. Finally, conclusions are drawn in Section 5.

2. Methodology

The LWDT requires a network of transducers to sequentially scan the plate, in which the transducers are used to transmit and receive Lamb wave signals. Using a pair of transducers as an example, Fig. 1 shows a schematic diagram of Lamb waves generated by a source transducer X_s, scattering at the damage region Σ_d, and then measured by the receiver transducer X_r. For a transducer network with N number of transducers, a number of the scattered wave signals can be collected from the sequential scan. The scattered wave signals are then used to reconstruct the damage using LWDT.

In this paper, the imaging algorithm used to reconstruct the damage is a near field imaging algorithm developed by Chan et el. [50]. This method was developed by extending the previously developed far-field imaging algorithm [28,41] to take into account the near field effect. In this section, we first describe the far-field imaging algorithm developed by Rose and Wang [28,41] and then presents the near-field algorithm [50].

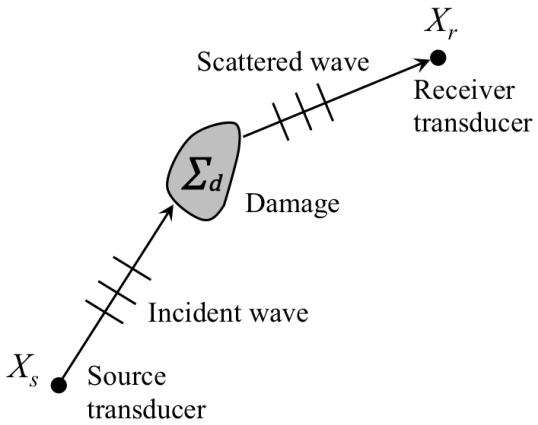

Fig.1: A schematic diagram of Lamb wave generation and scattering at damage

The far-field imaging algorithm with Born approximation [28] is appropriate for weak inhomogeneities in a plate. The Born approximation consists of approximating the total displacement with the incident wave displacement. The measured total displacement $\widehat{w}$ is given by the expression:

$$\hat{w} = \hat{w}^I + \hat{w}^S \tag{1}$$

where $\hat{w}^I$ is the incident wave displacement and $\hat{w}^S$ is the scattered wave displacement. The " ˆ " symbol means the frequency domain response obtained by the Fourier transform of the time-domain signal. Using the Born approximation, Eq. 1 becomes

$$\hat{w} = \hat{w}^I \tag{2}$$

The integral solution for a scattered field due to a defect can be represented by [28]:

$$\hat{w}^S(x,\omega) = \int\int k_1^2\, s(\xi)\hat{w}(x,\omega)G(x,\xi,\omega)d^2\xi \tag{3}$$

where k_1 denotes the wave number of the first flexural wave mode. $G(x,\xi,\omega)$ denotes the Green's function [41] of the scattered wave field from point ξ within the damage region Σ_d to point x on the plate. ω is the angular frequency. $s(\xi)$ is the damage potential that takes various physical forms depending on the nature of targeted damage. In this study, $s(\xi)$ is the reduced thickness within the damage boundary on the plate. Using the Born approximation, the total wave-field on the right-hand side of Eq. 3 can be replaced by the incident wave-field as

$$\hat{w}^S(x,\omega) = \int\int k_1^2\, s(\xi)\hat{w}^I(x,\omega)G(x,\xi,\omega)d^2\xi \tag{4}$$

Under far-field condition, the incident wave-field at ξ is given by:

$$\hat{w}^I(x,\omega) = e^{i\boldsymbol{k_1}^I\xi} \tag{5}$$

and the Green's function [41] is given by

$$G(x,\xi;\omega) = \frac{i}{4}\sqrt{\frac{2}{\pi k_1 r}}e^{i(k_1 r - \pi/4)}\, e^{-k_1{}^S\xi} \qquad \text{where} \quad k_1 r \to \infty \tag{6}$$

where $\boldsymbol{k}_1^I = k_1\alpha = k_1(cos\alpha, sin\alpha)$ is the incident wave vector. Inserting Eqs. 6 and 5 into Eq. 4, the integral representation for the scattered field becomes

$$\hat{w}^S(x,\omega) = \sqrt{\frac{i}{8\pi k_1 r}}e^{ik_1 r}A(\boldsymbol{k}_1^S, \boldsymbol{k}_1^I) \tag{7}$$

where $\boldsymbol{k}_1^S = k_1\theta = k_1(cos\theta, sin\theta)$ is the scattered wave vector. The physical significance of the Eq. 7 is the assumption that the damage is located at a distance from the PZTs, where the incident wave amplitude can be described by the plane-wave scattering amplitude.

$$A(\theta,\alpha;0) = \lim_{k_1 r\to\infty} \frac{\hat{w}^S(r,\theta;\omega)}{\sqrt{\frac{2}{\pi k_1 r}}e^{ik_1 r}e^{-i\pi/4}} \tag{8}$$

where $\hat{w}^S(r,\theta;\omega)$ is the scattered wave field along direction θ due to an incident plane-wave of unit strength in the direction α.

The fundamental concept of LWDT is to relate the 2D spatial Fourier Transform of the inhomogeneity variation to the plane-wave scattering amplitude. The inhomogeneity variation is eventually reconstructed by taking an Inverse Fourier transformation in the wavenumber space [43].

For plate-wave case, this inversion in the ***k***-space is formulated as integrals over the source and receiver angles:

$$s(x) = \frac{1}{8\pi^2}\int_0^{2\pi}\int_0^{2\pi}\frac{A(\theta,\alpha;0)}{q_h(\theta-\alpha)}|\sin(\theta-\alpha)|e^{ik_1(\theta-\alpha)x}d\theta d\alpha \quad (9)$$

where $s(x)$ denotes the reconstructed value of the plate thickness reduction δh. The term $|sin\ (\theta - \alpha)|$ is the Jacobian for the change in integration variables from $(k_x^S - k_x^I, k_y^S - k_y^I)$ to (θ, α). The parameter $q_h(\theta - \alpha)$ is a function of the type of damage chosen, which is plate thickness reduction in this case. It denotes the shape function characterising the scattering pattern for a point-scatterer and is given by the following expressions [43]. For a damage that is characterized by plate thickness reduction,

$$q_h = 3q_1 + q_2 + 3q_3 + q_4 \quad (10)$$

where

$$q_1(\Delta\theta) = \frac{\gamma_1 {k_1}^2}{({k_1}^2 - {k_2}^2)}[cos^2\Delta\theta + \nu\, sin^2\Delta\theta] \quad (11)$$

$$q_2(\Delta\theta) = \frac{\bar{\mu}h(1-\gamma_1)^2}{\gamma_1 D({k_1}^2 - {k_2}^2)}[\cos\Delta\theta] \quad (12)$$

$$q_3(\Delta\theta) = -\frac{\gamma_1\rho I\omega^2}{D({k_1}^2 - {k_2}^2)}[\cos\Delta\theta] \quad (13)$$

$$q_4(\Delta\theta) = -\frac{h\rho\omega^2}{\gamma_1 D{k_1}^2({k_1}^2 - {k_2}^2)} \quad (14)$$

where $\Delta\theta = \theta - \alpha$, or $\Delta\theta = \varphi_i - \varphi_j + \pi$ for the near field imaging formula, D denotes the bending stiffness of the plate, γ_1 is the wave amplitude ratio between the first and second branches of the wave mode. $k_{1,2}$ is the travelling and non-propagating wavenumber. $\bar{\mu}$ is the modified shear modulus. h is the plate thickness. ρ is the density of the plate material. ν is the Poisson ratio and I is the area moment of the vertical cross-section of the plate.

The near field algorithm [50] involves two major steps: i) the incident wave is expressed as a function of the vertical input force, ii) The plane wave scattering amplitude is expressed relative to the imaging point as opposed to the origin. When a vertical input force $\hat{F}(\omega)$ is applied by a transducer at location $X_s = (x_s, y_s)$, the incident wave generated by the transducer takes the following form as a function of its location x.

$$\hat{w}^I(x,\omega;X_s) = \hat{F}(\omega)G(x,\omega;X_s) \quad (15)$$

where $G(x, \omega; X_s)$ denotes the plate–wave dynamic Green's function. Fig. 2 shows a schematic diagram of a PZT network and imaging domain for the LWDT. Using Eq. 8, the scattered field at a receiving transducer location $X_r = (x_r, y_r)$ can be expressed as

$$\widehat{w}^S(x_r, y_r;\ \omega) = A\left(\varphi_{r,}\ \varphi_{s,} - \ \pi; x\right)\widehat{w}^I(x, \omega; X_s)\left(\frac{i}{4}\sqrt{\frac{2}{\pi k_1 r}}e^{ik_1\rho_r}e^{-i\pi/4}\right) \tag{16}$$

where $\widehat{w}^I$ is the incident wave given by Eq. 15 and ρ_r is the distance between a receiving sensor X_r and an imaging point x within the imaging domain. φ_r and φ_s are the receiver and source angles relative to the origin at the imaging point x as shown in Fig. 2. It can also be shown that the scattering amplitude relative to the origin at x can be related to the scattering amplitude relative to an origin at 0 by the following translation

$$A(\theta, \alpha; x) = A(\theta, \alpha; 0)e^{ik_1(\theta-\alpha)x} \tag{17}$$

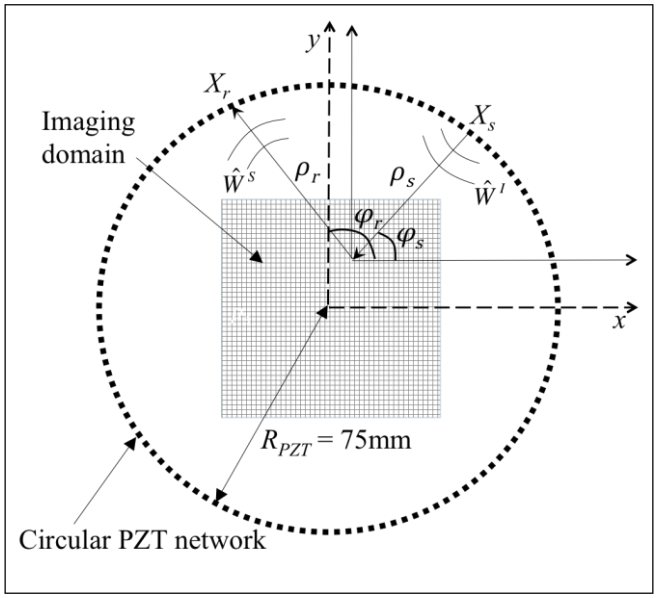

Fig. 2: A schematic diagram of the PZT configuration and imaging domain for Lamb wave diffraction tomography

In this paper, we only consider an analytical value for the Green's function [41] as opposed to the Green's function obtained from numerical method [50]. It has been shown that for flat plate, the Green's functions obtained using numerical methods are similar to the Green's functions obtained from the analytical method [50]. This analytical Green's function is given by [41]:

$$G(X_r, \omega; x) = \frac{1}{D\left(k_1{}^2 - k_2{}^2\right)\gamma_1}\frac{i}{4}\sqrt{\frac{2}{\pi k_1 r}}e^{ik_1\rho_r}e^{-i\frac{\pi}{4}} \tag{18}$$

Using Eq. 17 and 18, Eq. 9 can be rewritten in the following form:

$$s(x) = \frac{1}{8\pi^2 D\gamma_1\left(k_1{}^2 - k_2{}^2\right)}\int_0^{2\pi}\int_0^{2\pi}\frac{K_{rs}|\sin(\varphi_r - \varphi_s)|}{G(X_r, x)G(x, X_s)q_h(\varphi_r - \varphi_s + \pi)}d\varphi_r d\varphi_s \tag{19}$$

where

$$K_{rs} = \frac{\hat{w}^S(X_r,\omega;X_s)}{\hat{F}(\omega)} \quad (20)$$

represents the scattered field data normalized relative to the amplitude of the actuating force at the central frequency of the input tone-burst.

The inversion integral in Eq. 19 can be evaluated as a discrete sum of values using the trapezoidal quadrature rule. This is due to the finite number of source and receiver transducers that are used for generating the scattered field. Thus Eq. 19 can be expressed as:

$$s(x) = Re\left[\frac{1}{8\pi^2 D\gamma_1\left({k_1}^2-{k_2}^2\right)}\sum_{j=1}^{N}\sum_{i=1}^{N}\frac{K_{ij}\left|\sin(\varphi_i-\varphi_j)\right|}{G(X_i,x)G(x,X_j)q_h(\varphi_i-\varphi_j+\pi)}\Delta\varphi_i\Delta\varphi_j\right] \quad (21)$$

where $\Delta\varphi_i = (\varphi_{i+1} - \varphi_{i-1})/2$ in which $\varphi_0 = \varphi_N - 2\pi$. K_{ij} is the multi-static matrix defined by Eq. 20. φ is the polar angle relative to the imaging point *x* as origin. Subscripts *i* and *j* are used to identify receiver and source locations, respectively. *N* is the total number of source and receiver sensors. The value of the thickness reduction in the damage is thus obtained using Eq. 21.

This paper aims at examining the quality of the reconstructed damage image when the data at non-central frequencies is used to calculate the multi-static data matrix. This is carried out by taking the Fourier transform of the scattered field and extract the results at frequency that is $\pm N_f$ kHz away from the central frequency as shown in Fig. 3. It should be noted that care must also be taken in determining the corresponding value from the Fourier transform of the excitation force. In the next section the numerical case studies will be described in details, in which the effect of the data at each non-central frequency on the quality of the reconstructed damage image will be investigated.

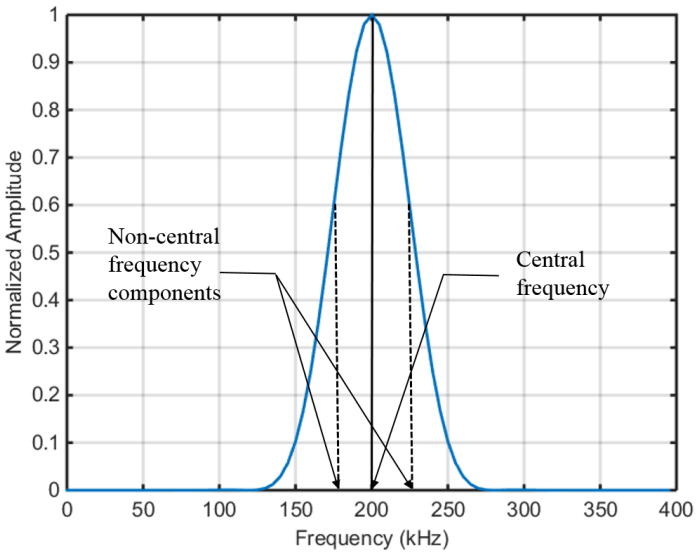

Fig 3: Central and non-central frequency components for a Lamb wave signal at 200 kHz (Solid line indicates central frequency and dashed lines indicate non-central frequencies)

3. Numerical Case Studies

The performance of the reconstructed damage image using non-central and central frequency components is investigated using a numerical simulation model of an isotropic aluminium plate. The three-dimensional (3D) explicit finite element (FE) method [48,49] is used to simulate Lamb wave scattering phenomenon at damage in an aluminium plate. A commercial FE software, ABAQUS, was used to carry out the FE simulations in this study. The size of the plate is 240 mm × 240 mm and the thickness is 1.6 mm. The Young's modulus is 69 GPa, density is 2760 kg/m^3 and Poisson's ratio ν = 0.33. The plate is modelled by eight-noded 3D reduced integration solid brick element (C3D8I) with incompatible modes. Each node of the solid brick element has three degrees-of-freedom (DoFs).

The fundamental anti-symmetric (A_0) Lamb wave is used as the incident wave and it is generated by transducers installed at the surface of the plate. In this study, only the deformations induced by the transducers are modelled, which is simulated by applying the out-of-plane nodal displacement at the required points. The excitation signal is a 200 kHz narrow-band five-cycle sinusoidal tone burst pulse modulated by a Hanning window. A circular transducer network, which contains 128 transducers, is used to actuate and measure the Lamb wave signals in this study. The radius of the circular transducer network is 10λ = 75 mm. The Lamb wave signals at particular locations are obtained by calculating the out-of-plane nodal displacement of the nodes located at the surface of the plate.

In the FE model, most of the solid brick elements have an in-plane square shape with dimensions 0.4 × 0.4 mm^2. This means that there are at least 12 nodes per wavelength and five layers of FE element in the thickness direction to ensure the accuracy of the Lamb wave simulation results. The model has six layers of elements along its thickness with the top and bottom layers having a height of 0.08 mm. The other four layers in between are of thickness 0.36 mm. The incremental time step of the explicit FE simulation is automatically controlled by ABAQUS based on the element size and material properties. Fig. 4 shows a comparison of the A_0 Lamb wave group velocity dispersion curve calculated by the FE simulations and analytical results, which is based on the Mindlin plate theory [48]. The results show that there is very good agreement between the FE calculated and analytical results. This shows that the FE simulations are able to accurately predict eh A_0 Lamb wave propagation in the plate.

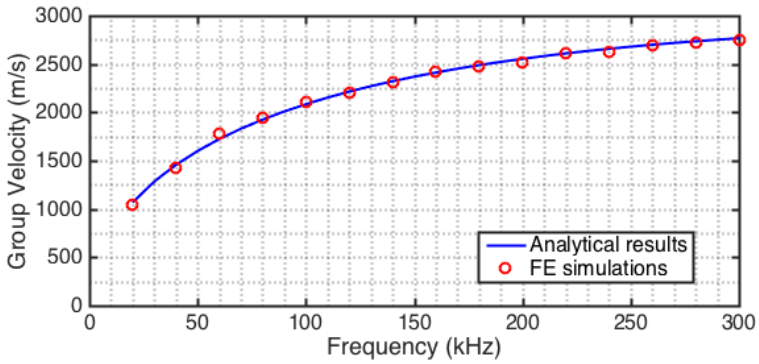

Fig. 4: A_0 Lamb wave group velocity dispersion curve

The imaging area is a 160 mm × 160 mm square as shown in Fig. 5. The plate thickness reduction damage is considered in this study, which is used to represent the common corrosion damage in metallic structure. The damage geometry is inscribed onto the surface of the model prior to its meshing. This ensures a uniform and structured meshing for the damage shape and helps to maintain a compatible mesh when the elements at the top layer within the damage geometry are removed to create the thickness reduction damage. Inscribing the model with the damage shape prior to its meshing ensures that tetrahedral elements are used near the edges of the damage and the circular shape is maintained even after the elements at the top layer are removed.

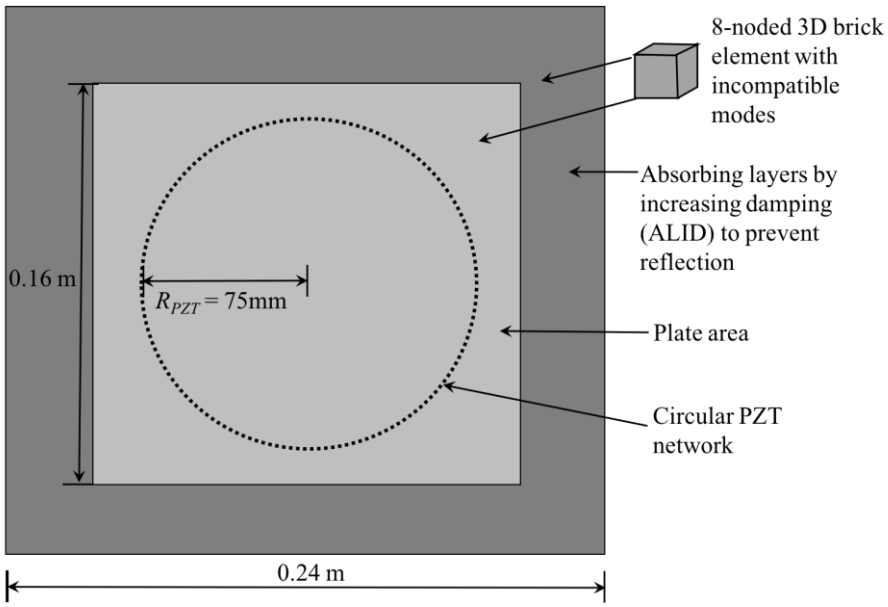

Fig. 5: Schematic of the finite element model and the PZT configuration

In the numerical simulation, the absorbing layer is used to minimise the computational cost of the FE simulation, and hence, the simulated model can represent a larger aluminium plate. In the FE model, absorbing layers by increasing damping (ALID) [51] is applied to four edges of the aluminium plate model as shown in Fig. 5. A high rate of variance in the damping coefficients

across the layers would give rise to stiff material layers that could themselves induce the wave reflections. A low rate of variance, on the other hand, would lead to an incomplete absorption of the incident wave, in which the boundary reflections are not fully eliminated in the simulation. It is thus imperative to vary the properties of the material gradually along these layers. The presence of an absorbing layer greatly reduces the dimension of the model to be analysed, while also eliminating any reflected waves simultaneously.

Each transducer was interrogated twice, in which one is to generate Lamb waves in an intact model and the other one is to generate Lamb waves in a model containing the damage. The scattered wave-field is then obtained by subtracting the baseline response the intact model from the total response obtained of the damaged model. The scatter field is gathered from the locations of each of the transducers and aids in constructing a single row of the multi-static data matrix K_{ij}. This process is repeated for every transducer to obtain an $N \; x \; N$ matrix where N is the number of transducers. The diffraction tomography process requires each of the N transducers to be stimulated sequentially in order to obtain the multi-static data matrix.

The numerical studies were carried out, which considers thickness reduction damage. This paper focuses on the efficiency of various central and non-central frequencies in predicting the damage parameters for different shapes of damages. To provide a robust comparison, the damages considered in this study are located at the same location. The three cases considered in this paper are a) a circular shaped damage b) a cross shaped damage, and c) a square shaped damage. Using the circular shaped damage as an example, the damage is modelled as a symmetric reduction in thickness at both surfaces of the plate as shown in Fig. 6b. This prevents any mode-conversion [52] of waves at the damage and ensures that the scattered field consists of only the A_0 mode Lamb wave. A 10% reduction of thickness is considered in all the aforementioned cases. The image will be reconstructed at the central frequency of 200 kHz as well as at frequencies ± 20 kHz away from the central frequency.

3.1. Circular damage

The first case consists of a circular damage of diameter 12 mm (~ 1.5λ) located at the origin of the plate as shown in Fig. 6. Owing to symmetry of shape and location of the damage, the simulation of Lamb wave generation and scattering can be simplified to excitation of just one PZT. This is because the excitation of every PZT in this configuration yields the same scattered field. However, care must be taken while assembling the multi-static data matrix using Eq. 20, as the order of the elements in each row depends on order and location of the PZT excited.

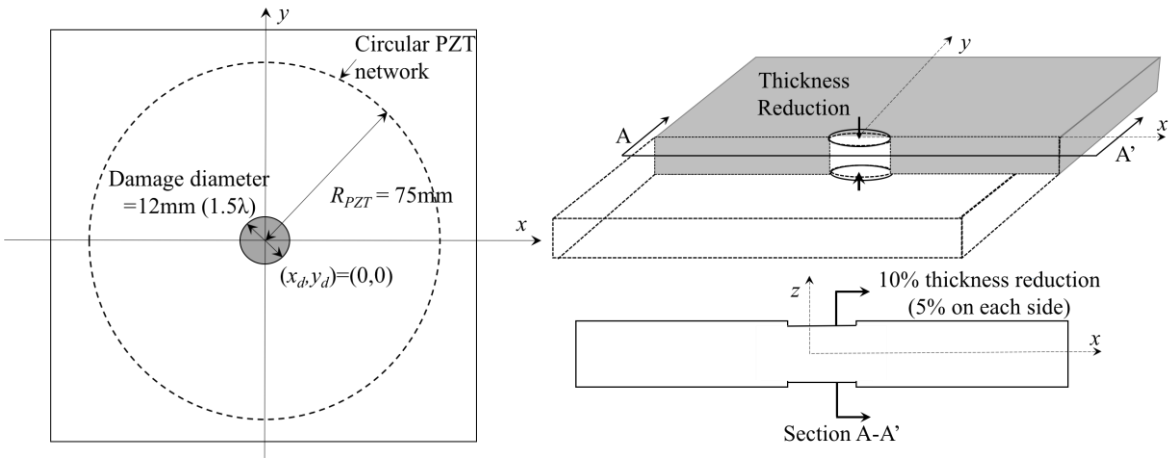

(a) (b)

Fig. 6: a) Schematic of the circular thickness reduction damage b) cross-section view

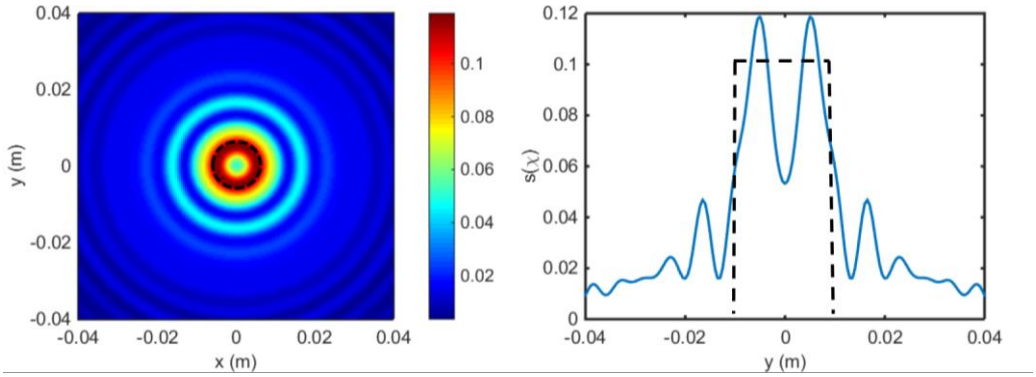

(a) (b)

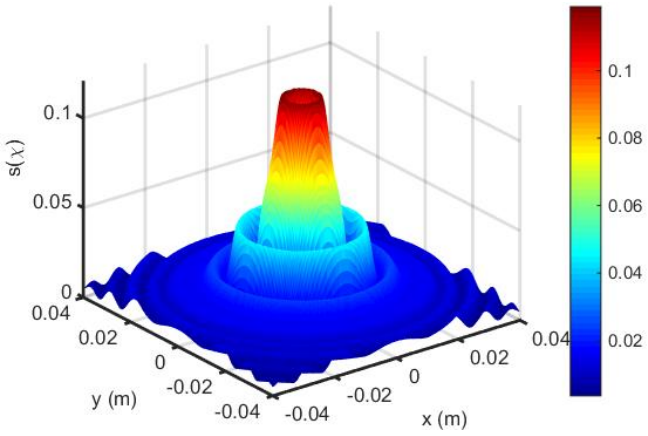

(c)

Fig. 7: Damage reconstruction of circular damage for the central frequency of 200 kHz a) 2-D variation of damage along the surface of the plate, b) damage profile along the line $x = 0$, c) 3-D variation of damage (Dashed lines indicate the true geometry and thickness reduction value of the damage)

The results obtained using the algorithm, are found in Figs. 7-9. The damage reconstruction was performed using the central frequency of 200 kHz, and the non-central frequencies of 180 kHz and 220 kHz. The damage reconstruction obtained using the central frequency was found to be accurate in its prediction of the thickness reduction but it was less satisfactory in its reconstruction of the damage geometry (Fig. 7). Figs. 8 and 9 show that the use of non-central frequencies gives an excellent reconstruction of the damage shape and size. However, they were less satisfactory in their prediction of the thickness reduction. It is worth mentioning that for non-central frequencies, while calculating the multi-static data matrix K_{ij} using the scatter data, care was taken to choose the corresponding non-central frequency in the amplitude of the actuating force as shown in Eq. 20.

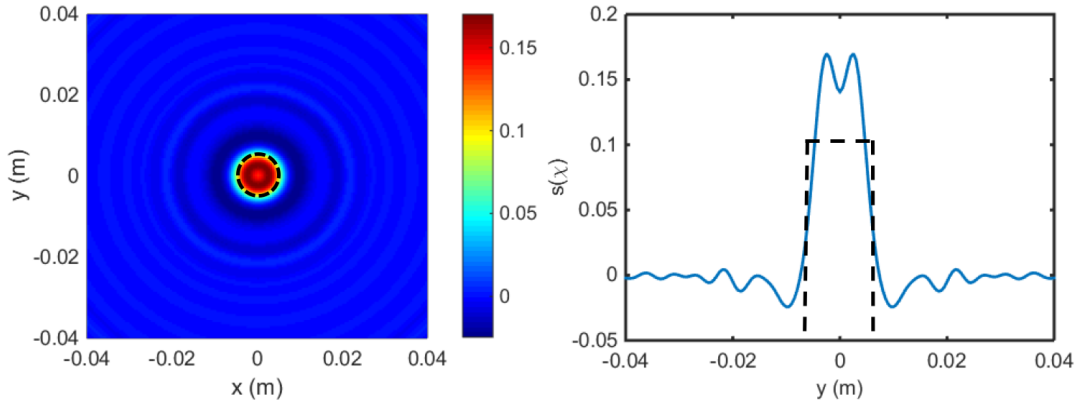

(a) (b)

Fig. 8: Damage reconstruction for a non-central frequency of 220 kHz a) 2-D variation, b) damage profile along the line $x = 0$

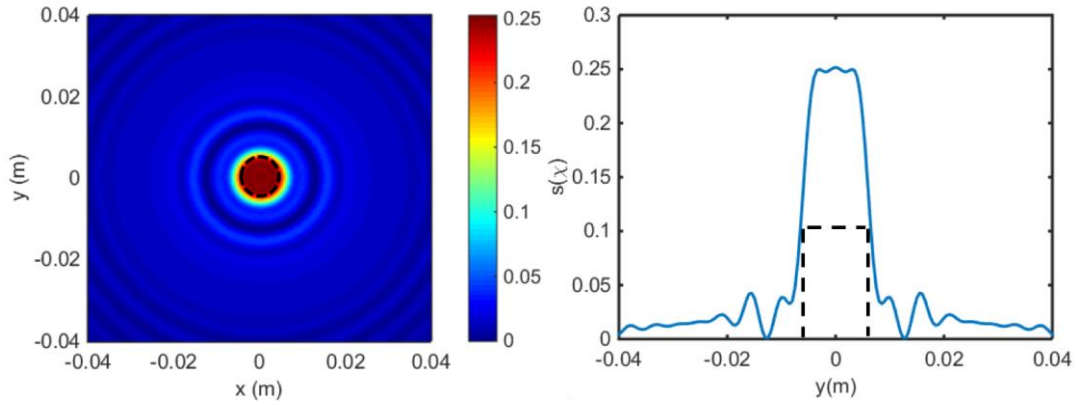

(a) (b)

Fig. 9: Damage reconstruction for a non-central frequency of 180 kHz a) 2-D variation b) damage profile along the line $x = 0$

3.2. Cross shaped damage

The second case consists of a cross shaped damage, located at the origin of the plate. The width of the intersecting bars is 2 mm and the total width of the cross shaped damage is 12 mm. The cross shaped damage is symmetric in each quadrant as shown in Fig. 10, and hence, the FE simulation can be simplified to only simulating the excitation of the 32 PZTs in the first quadrant. The results for the other 96 PZTs can be obtained by carefully rearranging the data obtained from these simulations.

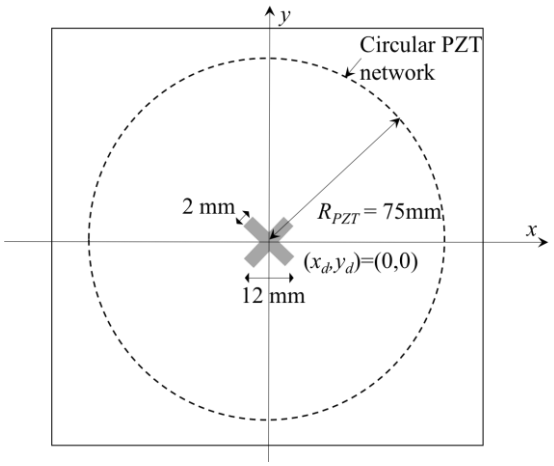

Fig. 10: Schematic of the geometry, location and dimensions of the cross shaped thickness reduction damage

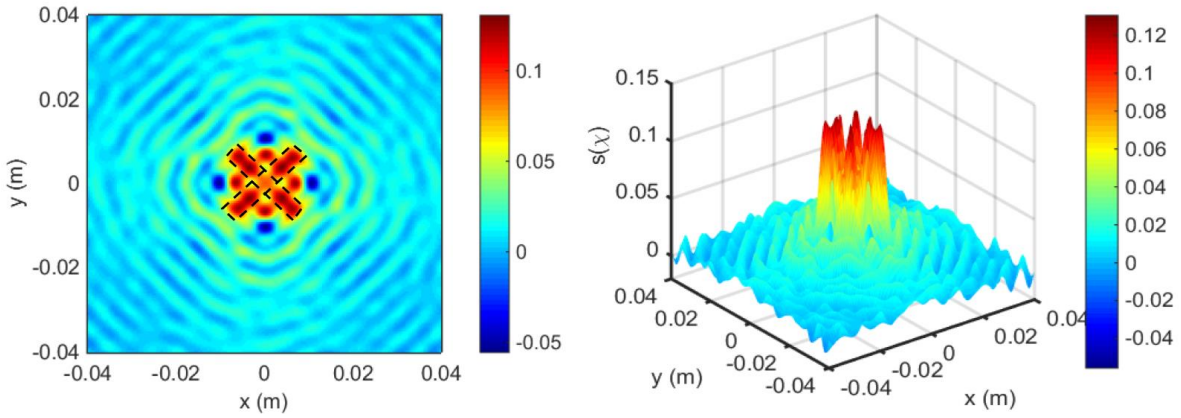

(a) (b)

Fig. 11: Damage reconstruction of the cross shaped damage for the central frequency of 200 kHz a) 2-D variation along the surface of the plate, b) 3-D variation along the surface of the plate (Dashed lines indicate the true geometry and thickness reduction value of the damage)

The results obtained using the imaging algorithm, are shown in Figs. 11 and 12. The damage reconstruction obtained using the central frequency was found to be accurate in its prediction of the thickness reduction. However, there are still some discrepancies between the reconstructed shape

and the actual shape of the damage as shown in Fig. 11. The additional peaks between the intersecting bars can be attributed to the irregular meshing that is the result of the sharp and irregular corners in the structure. The effect of these corners can also be seen in the damage reconstruction image (Fig. 12) using non-central frequencies but with lesser extent. In general, the use of non-central frequencies provides better prediction of the damage shape but the reconstructed image is less accurate in predicting the thickness reduction as well as the damage size.

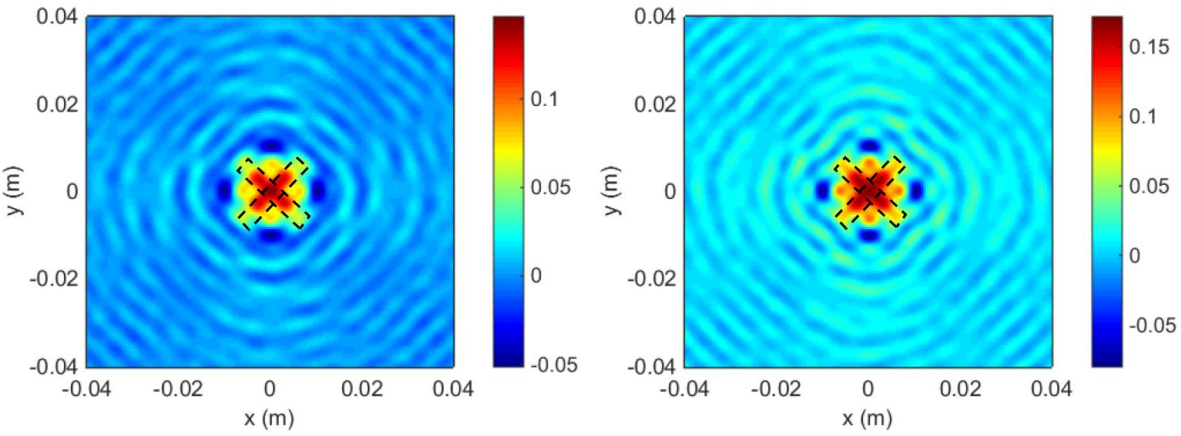

(a) (b)

Fig. 12: 2-D damage reconstruction of the cross shaped damage for non-central frequencies of a) 220 kHz, b) 180 kHz

3.3. Square shaped damage

The final case consists of square shaped damage with 12 mm wide at each side, and it is located at the origin of the plate. The same as cross shaped damage case, the square shaped damage is also symmetric in each quadrant, and hence, it be simplified to simulate only 32 PZTs. The results obtained using the imaging algorithm are shown in Figs. 13 and 14. The reconstructed images for the square shaped thickness reduction damage were found to be accurate in predicting the damage geometry and size. Although the difference in the prediction of damage geometry using both central and non-central frequencies was not as significant as in the previous cases, there was still a relatively large difference in predicting the thickness reduction. This means the performance of imaging algorithm in predicting the thickness reduction is not as good as the damage geometry and size prediction.

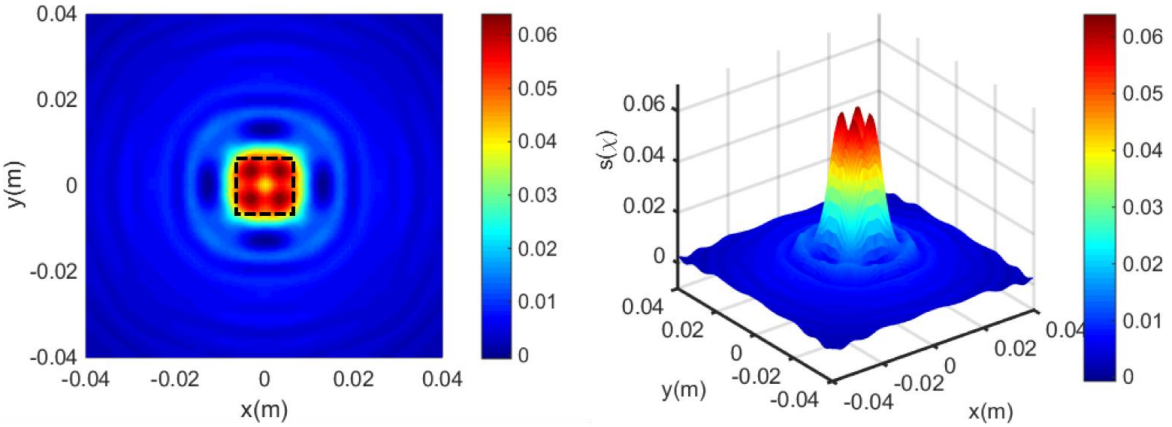

(a) (b)

Fig. 13: Damage reconstruction of the square shaped damage for the central frequency of 200 kHz a) 2-D variation along the surface of the plate, b) 3-D variation along the surface of the plate (Dashed lines indicate the true geometry and thickness reduction value of the damage)

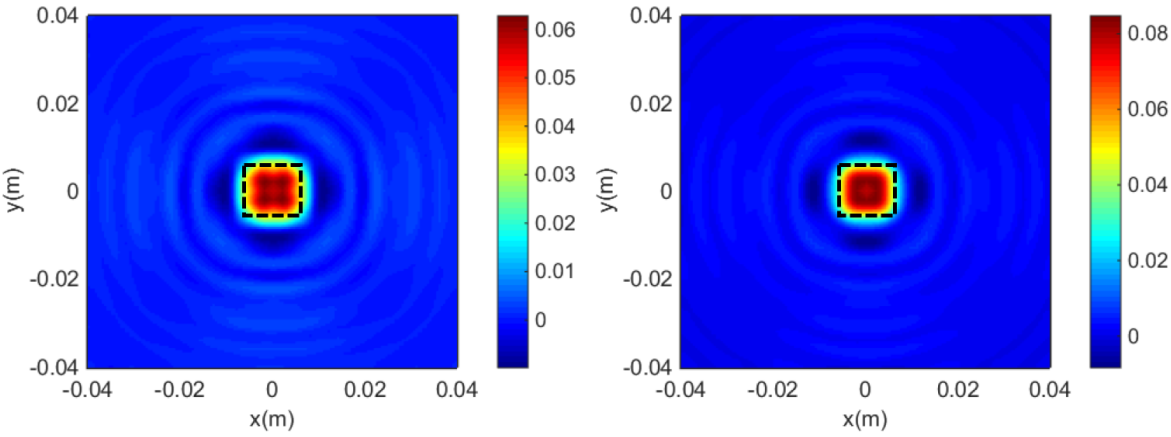

(a) (b)

Fig. 14: 2-D damage reconstruction of the square shaped damage for non-central frequencies of a) 220 kHz, b) 180 kHz

4. Conclusions

This study has investigated the performance of the LWDT in reconstructing different shapes of damage using central and non-central frequencies. A series of numerical case studies have been carried out using the 3D FE simulations. The results show that the scattering data at the non-central frequencies can also be used to reconstruct damage using LWDT. This means the non-central frequencies could provide addition information in the reconstruction of damage image. This can be attributed to the additional important information regarding the damage geometry, size or the magnitude of damage contained by each additional non-central frequency. One of the main inferences of this study is that the symmetric frequencies on either side of the central frequency

provide different results in the reconstruction of the damage image. This can aid in recognising that the most efficient interval for studying multi-frequency approaches of damage reconstruction, i.e., the non-central frequency components around the centre of the frequency spectrum. The results also reconfirms that the most accurate estimations of the damage parameters are indeed obtained from the central frequencies.

In this study, it has been shown that although the central frequencies are the best sources of information in estimating the magnitude of the thickness reduction, the non-central frequencies are still helpful and can provide additional information in the image reconstruction. The quality of the damage reconstruction was found to be significantly better for regular and symmetric geometries of thickness reduction damage that do not contain sharp edges and corners. It can be observed in cross shaped damage case that while the deficiencies of the meshing and sharp corners are magnified for the central frequency, they are significantly diminished for the non-central frequencies. Hence, one can consider an increased weighting of the contribution of non-central frequency components in the reconstruction of damage image. Efforts are currently exploiting the use of multi-frequency information in the LWDT so that the quality of the reconstructed image can be further improved.

Acknowledgement

The research described in this paper was financially supported by the Australian Research Council under grant number DE130100261. The support is greatly appreciated.

References

1. Forsyth DS, Komorowski JP, Gould RW, Marincak A. (1998). Automation of enhanced visual NDE techniques. *Proceeding of the 1st Pan-American Conference for NDT, Toronto, Canada*, 107–117.
2. Komorowski JP, Forsyth DS. (2000). The Role of enhanced visual inspections in the new strategy for corrosion management. *Aircraft Engineering and Aerospace Technology*, 71(1):5-13.
3. Blitz J and Simpson G. (1995). Ultrasonic methods of non-destructive testing, Springer Netherlands.
4. Schmerr LW, Song JS. (2007). Ultrasonic nondestructive evaluation systems. Springer US.
5. Kobayashi K, Banthia N. (2011). Corrosion detection in reinforced concrete using induction healing and infrared thermography. *Journal of Civil Structural Health Monitoring*, 1:25-35.
6. Hiasa S, Birgul R, Catbas FN. (2016) Infrared thermography for civil structural assessment: demonstrations with laboratory and field studies. *Journal of Civil Structural Health Monitoring*, 6:619-636.

7. Lepine BA, Giguere JSR, Forsyth DS, Chahbaz A, Dubois JMS (2002) Interpretation of pulsed eddy current signals for locating and quantifying metal loss in thin skin lap splices. *AIP Conference Proceeding*, 615(1):415-422.
8. Lepine BA, & Holt RT. (1997). An eddy current scanning method for the detection of corrosion under fasteners in thick skin aircraft structures. *Canadian Aeronautics and Space Journal*, 43(1):28-33.
9. Torres-Arredondo MA, Buethe I, Tibaduiza DA, Rodellar J, Fritzen CP. (2013). Damage detection and classification in pipework using acousto-ultrasonics and non-linear data-driven modelling. *Journal of Civil Structural Health Monitoring*, 3(4):297-306.
10. Gulizzi V, Rizzo P, Milazzo A, Malfa Ribolla EL. (2015). An integrated structural health monitoring system based on electromechanical impedance and guided ultrasonic waves. *Journal of Civil Structural Health Monitoring*, 5(3):337-352.
11. He S, Ng CT. (2017). Modelling and analysis of nonlinear guided wave interaction at a breathing crack using time-domain spectral finite element method. *Smart Materials and Structures*, 26(085002).
12. Yang Y, Ng CT, Kotousov A, Sohn H, Lim HJ. (2018). Second harmonic generation at fatigue cracks by low-frequency Lamb waves: Experimental and numerical studies. *Mechanical Systems and Signal Processing*, 99:760-773.
13. Ng CT. (2014). On the selection of advanced signal processing techniques for guided wave damage identification using a statistical approach. *Engineering Structures*, 67: 50-60.
14. Kurt I, Akbarov SD, Sezer S. (2016). The influence of the initial stresses on Lamb wave dispersion in pre-stressed PZT/Metal/PZT sandwich plates. *Structural Engineering & Mechanics*, 58: 347-378.
15. He S, Ng CT. (2015). Analysis of mode conversion and scattering of guided waves at cracks in isotropic beams using a time-domain spectral finite element method. *Electronic Journal of Structural Engineering*, 14:20-32.
16. Giurgiutiu V, Bao J. (2004). Embedded-ultrasonics structural radar for in situ structural health monitoring of thin-wall structures. *Structural Health Monitoring*, 3(2):121-140.
17. Aryan P, Kotousov A, Ng CT, Cazzolato B. (2017). A model-based method for damage detection with guided waves. *Structural Control and Health Monitoring*, 24(3):e1884.
18. Quek ST, Tua PS, Wang Q. (2003). Detecting anomalies in beams and plate based on the Hilbert–Huang transform of real signals. *Smart Materials and Structures*, 12(3):447-460.
19. Flynn EB, Todd MD, Wilcox PD, Drinkwater BW, Croxford AJ. (2011). Maximum-likelihood estimation of damage location in guided-wave structural health monitoring. *Proceedings of the*

Royal Society of London A: Mathematical, Physical and Engineering Sciences, 467(2133):2575-2596.

20. Aryan P, Kotousov A, Ng CT, Cazzolato BS. (2017). A baseline-free and non-contact method for detection and imaging of structural damage using 3D laser vibrometry. *Structural Control and Health Monitoring*, 24(4):e1894.
21. Tian Z, Yu L, Leckey C, Seebo J. (2015). Guided wave imaging for detection and evaluation of impact-induced delamination in composites. *Smart Materials and Structures*, 24(10):105019.
22. Zhao X, Gao H, Zhang G, Ayhan B, Yan F, Kwan C, Rose JL. (2007). Active health monitoring of an aircraft wing with embedded piezoelectric sensor/actuator network: I. Defect detection, localization and growth monitoring. *Smart materials and structures*, 16(4), 1208-1217.
23. Purekar AS, Pines DJ, Sundararaman S, Adams DE. (2004). Directional piezoelectric phased array filters for detecting damage in isotropic plates. *Smart Materials and Structures*, 13(4): 838-850.
24. He S, Ng CT. (2016). A probabilistic approach for quantitative identification of multiple delaminations in laminated composite beams using guided waves. *Engineering Structures*, 127:602-614.
25. He S, Ng CT (2017) Guided wave-based identification of multiple cracks in beams using a Bayesian approach. *Mechanical Systems and Signal Processing*, 84(1):324-345.
26. Sohn H, Park HW, Law KH, Farrar CR. (2007). Damage detection in composite plates by using an enhanced time reversal method. *Journal of Aerospace Engineering*, 20(3):141-151.
27. Malyarenko EV, Hinders MK. (2001). Ultrasonic Lamb wave diffraction tomography. *Ultrasonics*, 39(4):269-281.
28. Wang CH, Rose LRF. (2003). Plate-Wave Diffraction Tomography for Structural Health Monitoring. *AIP Conference Proceedings*, 657(1):1615-1622.
29. Ng CT. (2015). A two-stage approach for quantitative damage imaging in metallic plates using Lamb waves, *Earthquakes and Structures*, 8(4):821-841.
30. Pruell C, Kim JY, Qu J, Jacobs LJ (2009) Evaluation of fatigue damage using nonlinear guided waves. *Smart Materials and Structures*, 18(3):035003.
31. Dutta D, Sohn H, Harries KA, Rizzo P (2009) A nonlinear acoustic technique for crack detection in metallic structures. *Structural Health Monitoring*, 8(3):251-0262.
32. Soleimanpour R, Ng CT, Wang CH (2017) Higher harmonic generation of guided waves at delaminations in laminated composite beams. *Structural Health Monitoring*, 16(4):400-417.
33. Shen Y, Cesnik CES (2017) Modeling of nonlinear interactions between guided waves and fatigue cracks using local interaction simulation approach. *Ultrasonics*, 74:106-123.

34. Soleimanpour R, Ng CT (2017) Locating delaminations in laminated composite beams using nonlinear guided waves. *Engineering Structures*, 131:207-219.
35. Konstantinidis G, Drinkwater BW, Wilcox PD (2006) The temperature stability of guided wave structural health monitoring systems. *Smart Materials and Structures*, 15(4):967-976.
36. Aryan P, Kotousov A, Ng CT, Wildy S (2016). Reconstruction of baseline time-trace under changing environmental and operational condition. *Smart Materials and Structures*, 25(3):035018.
37. Mohabuth M, Kotousov A, Ng CT (2016) Effect of uniaxial stress on the propagation of higher-order Lamb wave modes. *International Journal of Nonlinear Mechanics*, 86:104-111.
38. Jansen DP, Hutchins DA. (1990). Lamb wave tomography, *IEEE 1990 Ultrasonics Symposium*, 2:871-874.
39. Malyarenko EV, Hinders MK. (2000). Fan beam and double crosshole Lamb wave tomography for mapping flaws in aging aircraft structures. *The Journal of the Acoustical Society of America*, 108(4):1631-1639.
40. Leonard KR, Malyarenko EV, Hinders MK. (2002). Ultrasonic Lamb wave tomography. *Inverse Problems*, 18(6):1795-1808.
41. Rose LRF, Wang CH. (2004). Mindlin plate theory for damage detection: Source solutions. *The Journal of the Acoustical Society of America*, 116(1):154-171.
42. Belanger P, Cawley P, Simonetti F. (2010). Guided wave diffraction tomography within the born approximation. *IEEE Transactions on Ultrasonics, Ferroelectrics, and Frequency Control*, 57(6):1405-1418.
43. Rose LF, Wang CH. (2010). Mindlin plate theory for damage detection: imaging of flexural inhomogeneities. *The Journal of the Acoustical Society of America*, 127(2):754-763.
44. Huthwaite P, Simonetti F. (2013). High-resolution guided wave tomography. *Wave Motion*, 50(5):979-993.
45. Huthwaite P. (2014). Evaluation of inversion approaches for guided wave thickness mapping. *Proceedings of the Royal Society of London A: Mathematical, Physical and Engineering Sciences*, 470(2166):20140063.
46. Devaney AJ, Dennison M. (2003). Inverse scattering in inhomogeneous background media. *Inverse Problems*, 19(4):855-870.
47. Rohde AH, Rose LRF, Veidt M, Wang CH. (2009). Two inversion strategies for plate wave diffraction tomography. *Materials Forum*, 33:489-495.
48. Ng CT. (2015). On accuracy of analytical modelling of Lamb wave scattering at delaminations in multilayered isotropic plates. *International Journal of Structural Stability and Dynamics*, 15(8): 1540010.

49. Soleimanpour R, Ng CT. (2016). Scattering of the fundamental anti-symmetric Lamb wave at through-thickness notches in isotropic plate. *Journal of Civil Structural Health Monitoring*, 6:447-459.
50. Chan E, Rose LF, Wang CH. (2015). An extended diffraction tomography method for quantifying structural damage using numerical Green's functions. *Ultrasonics*, 59:1-13.
51. Rajagopal P, Drozdz M, Skelton EA, Lowe MJS, Craster RV. (2012) On the use of absorbing layers to simulate the propagation of elastic waves in unbounded isotropic media using commercially available Finite Element packages. *NDT & E International*, 51:30–40.
52. Ng CT. (2014). Bayesian model updating approach for experimental identification of damage in beams using guided waves. *Structural Health Monitoring*, 13(4): 359-373.